Excited state and charge dynamics of hybrid organic/inorganic heterojunctions. II. Experiment

Anurag Panda,[1] C. Kyle Renshaw,[2] Ardavan Oskooi,[3] Kyusang Lee,[3] and Stephen R. Forrest[1,2,3]
[1]*Department of Materials Science and Engineering, University of Michigan, Ann Arbor, Michigan 48109, USA*
[2]*Department of Physics, University of Michigan, Ann Arbor, Michigan 48109, USA*
[3]*Department of Electrical Engineering and Computer Science, University of Michigan, Ann Arbor, Michigan 48109, USA*
(Received 27 April 2014; published 9 July 2014)

In our companion paper (Paper I) [C. K. Renshaw and S. R. Forrest, Phys. Rev. B **90**, 045302 (2014)], we developed a model for charge transport and photogeneration at hybrid organic/inorganic semiconductor heterojunctions (OI-HJs). Here we apply the model to two planar bilayer hybrid photovoltaic devices: the first using the wide-band gap n-TiO_2 in combination with the hole transporting tetraphenyl-dibenzoperiflanthene (DBP), and the second based on the moderate-band gap n-InP and the hole transporting pentacene (PEN). We measure the external quantum efficiency (EQE) and current density vs voltage (J-V) characteristics of both devices as functions of temperature. The EQE spectra for both TiO_2/DBP and InP/PEN provide convincing evidence that Frenkel states generated in the organic form hybrid charge transfer excitons (HCTEs) at the OI-HJ that are subsequently dissociated into free charges, and then collected at the opposing electrodes. The dissociation efficiency is found to be strongly influenced by the presence of surface states, particularly in the InP/PEN device. We further develop the J-V model from Paper I to include an analytical expression for space-charge effects in the organic at high currents. Model fits to the J-V data suggest that the temperature-dependent hole mobilities in both DBP and PEN result in increasing space-charge effects at low temperatures. Furthermore, we find that the J-V characteristics of the TiO_2/DBP device both in the dark and under illumination are governed by interface recombination. In contrast, the dark current in the InP/PEN device is governed by injection over the OI-HJ barrier, whereas the photocurrent is dominated by interface recombination. This work elucidates the role of the HCTE state in photogeneration, and the applicability of our model to a range of important optoelectronic devices.

DOI: 10.1103/PhysRevB.90.045303 PACS number(s): 73.40.−c, 78.66.−w, 81.05.Fb

I. INTRODUCTION

Previously (Paper I) [1], we presented a theoretical model describing exciton and charge dynamics at hybrid organic/inorganic semiconductor heterojunctions (OI-HJs). We proposed that the dark and illuminated electrical characteristics of OI-HJ diodes are determined by junction properties such as energy level offsets between the two materials, the magnitude and density of states of the interface traps, and the properties of the hybrid charge transfer exciton (HCTE). In the dark, recombination of injected electrons and holes occurs primarily at the OI-HJ through a HCTE-like state. When illuminated, the HCTE is also formed following the diffusion of a Frenkel-like exciton from the organic to the OI-HJ. Dissociation of the HCTE results in free carriers that are collected at the electrodes. Conversely, illumination of the inorganic directly yields free charge which results in minority carrier injection over the OI-HJ where it can potentially recombine. Due to the importance of interface recombination, interface trap states and the charge mobility in the organic were found to strongly influence the calculated current density vs voltage (J-V) characteristics of the hybrid diodes.

In this work, we apply the model of Paper I to understand the photo- and dark-current characteristics of two archetype OI-HJs. One is based on the wide-band gap TiO_2/tetraphenyldibenzoperiflanthene (DBP) acceptor junction. TiO_2 has found widespread use in OI dye-sensitized solar cells [2,3] and has been recently explored in metal oxide polymer HJ solar cells [4,5]. Furthermore, Frenkel–Wannier-Mott exciton hybridization has been found in the closely related metal oxide semiconductor/organic system consisting of ZnO and 3,4,7,8 naphthalenetetracarboxylic dianhydride in strongly coupled optical cavities [6]. The second system studied here is the moderate-band gap InP/pentacene (PEN) junction. Among other applications, InP has been shown to form rectifying OI-HJs [7,8] that result in an improved photovoltaic power conversion efficiency compared to cells lacking an organic window layer [9]. The characteristics of these two systems as functions of temperature (T) provide insight into the nature of the HCTE and the role of surface states in determining the diode properties.

Resonant and nonresonant energy and charge transfer between organic and inorganic materials have been studied by various groups. Specifically, the potential for exciton transfer across the OI-HJ through Förster resonant energy transfer (FRET) has been theoretically explored by Agranovich *et al.* [10] and experimentally by Itskos *et al.* [11] and Blumstengel *et al.* [12]. By placing a quantum well (QW) in the inorganic near the OI-HJ, FRET was found to be efficient in some systems but highly dependent on the distance of the QW from the OI-HJ. Studies of exciton dissociation through charge transfer at the OI-HJ have been complicated by chemical reaction of organic molecules with unpassivated inorganic surfaces [13,14] and exciton quenching by surface states. Nevertheless, exciton dissociation at HJs between inorganic quantum dots and organic molecules [15], and TiO_2 and various organic dyes [3], has been reported in the absence of surface states. Transient response studies of OI-HJs between organic polymers and CdS [16] or ZnO [17] have also confirmed the existence of a bound state at the interface. To understand the range of phenomena observed for these OI-HJs based on a variety of organic and inorganic semiconductors, it would be beneficial to have more comprehensive studies

1098-0121/2014/90(4)/045303(12) ©2014 American Physical Society

combining both theory and experiment that elucidate the role of the HCTE in determining the optical and electrical properties of OI-HJ diodes.

Here, we quantitatively analyze both the external quantum efficiency (EQE) and J-V characteristics of archetype OI-HJs as functions of T. When coupled with the theory in Paper I, the analysis provides convincing evidence for the existence of an HCTE in both the InP and TiO_2-based systems. Furthermore, the HCTE at the InP/PEN junction is strongly affected by traps at high temperatures. At low temperatures, the trap effects are "frozen out," resulting in a significant reduction in exciton quenching at the OI-HJ. In contrast, traps play a reduced role at the TiO_2/DBP junction. Fits to the J-V characteristics under both illumination and in the dark show the relative importance of charge injection over the OI-HJ barrier vs interface recombination in the two systems. By comparing the EQE and J-V data from these two cases, we test the validity and generality of the comprehensive theory presented in Paper I.

This paper is organized as follows: In Sec. II we extract and modify results from Paper I that are relevant to the specific cases of wide and moderate band gap semiconductor systems studied here. In Sec. III, we provide experimental details, with results in Sec. IV. In Sec. V, these results along with their broader implications to the physics of OI-HJs are discussed in the context of the theory. Section VI presents our conclusions. Since the excited state and charge recombination kinetics are significantly different for the wide- and moderate-band gap semiconductor systems, wherever necessary our discussion is divided into subsections that treat these two cases separately.

II. THEORY

The fundamental theory for charge and exciton transport dynamics at OI-HJs has been thoroughly described in Paper I. Here, we modify the theory to provide a description of these properties for the specific cases of the wide- and moderate-band gap semiconductor devices studied in this work.

The process of photon absorption to charge extraction in an OI-HJ is markedly different for the organic and inorganic semiconductors, as illustrated in Fig. 1 for the organic semiconductor. Photon absorption within the organic film generates a tightly bound exciton which then diffuses to the OI-HJ [Figs. 1(a) and 1(b)]. There, the electron transfers to the inorganic through either a resonant or nonresonant process, depending on the relative magnitudes of the organic and inorganic energy gaps, and their offsets (i.e., type I, II, or III) [18]. This results in the formation of an HCTE whose stability is primarily determined by the permittivities of the contacting materials [Fig. 1(c)] and the effective mass of the electron in the inorganic [cf. Fig. 2(b), Paper I]. The HCTE then dissociates and the hole and electron are collected at the electrodes [Fig. 1(d)], returning the organic back to its ground state [Fig. 1(e)]. If there is a high density of interface traps, the HCTE and/or its excitonic precursor can rapidly recombine. In cases where the band gap of the inorganic is lower than the exciton energy in the organic, the exciton can potentially Förster transfer to the inorganic [11], thereby circumventing the formation of the HCTE. In contrast, photon absorption in the inorganic leads directly to free carrier generation. To be collected at the electrode, the minority carrier must traverse the OI-HJ and transport through the organic. If the minority carrier diffusion length in the inorganic is greater than the layer thickness, the collection efficiency is limited by interface recombination. Hence, both the relative magnitudes of the organic and inorganic band gaps, the magnitude of the OI-HJ energy offset, and the presence of interface traps determine the charge generation dynamics.

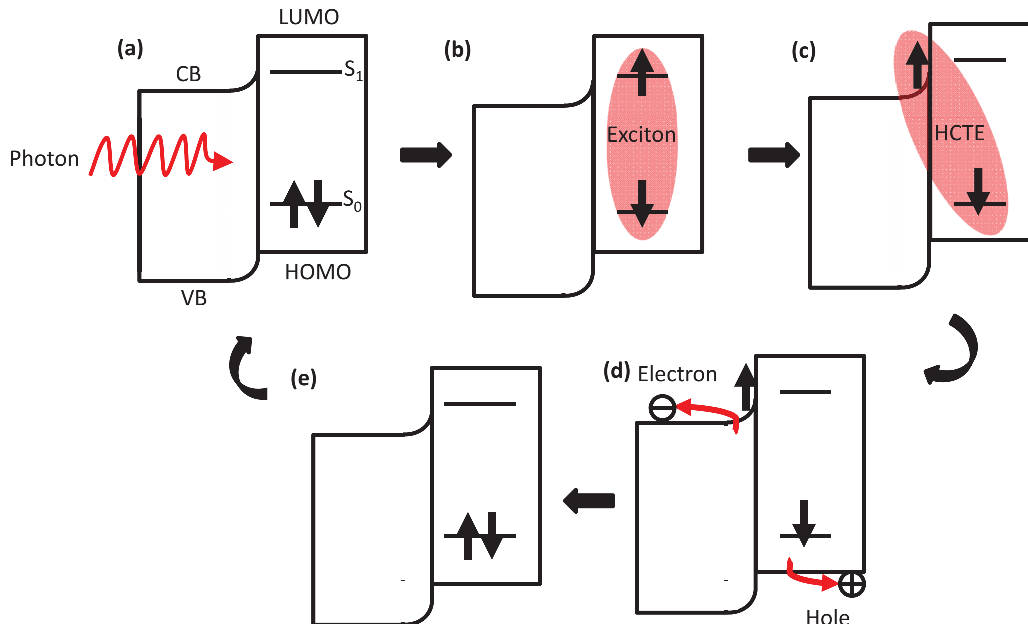

FIG. 1. (Color online) The process of charge generation via the generation of excitons in the organic semiconductor of an organic/inorganic heterojunction (OI-HJ) device. (a) Photon absorption in the organic; (b) exciton formation; (c) hybrid charge transfer exciton (HCTE) formation at the OI-HJ following exciton diffusion; (d) exciton dissociation and charge extraction; and (e) return of the organic to the ground state (S_0). Here, S_1 is the first singlet excited state of the organic.

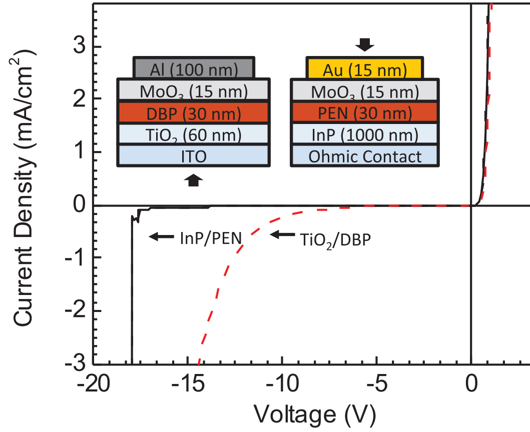

FIG. 2. (Color online) Current-voltage characteristics showing the breakdown of an InP/pentacene (PEN) diode (solid line) and a TiO_2/tetraphenyldibenzoperiflanthene (DBP) diode (dashed line) at −18 and −14 V, respectively. The device structures are shown in the inset, where the arrows indicate illumination direction.

A rigorous treatment of exciton and charge dynamics at the OI-HJ requires simultaneous solution to the coupled drift-diffusion and Poisson's equations for both the inorganic and organic layer [1]. To simplify this analysis, we begin by recognizing that the mobility of the inorganic ($\mu\sim 1$–$10\,000\ \mathrm{cm^2/V\,s}$) [19–22] is generally large compared to that of the organic semiconductor ($\mu\sim 1$–$10^{-7}\ \mathrm{cm^2/V\,s}$) [23,24], such that we can assume that the quasi-Fermi energy is flat throughout the inorganic layer (cf. Sec. II B, Paper I). To calculate the quasi-Fermi energy in the organic we assume that drift is the dominant mechanism for charge transport at high voltages [25]. Hence, we combine the equilibrium and nonequilibrium solutions in Paper I to obtain the hole density on the organic side of the OI-HJ:

$$P_{\mathrm{HJ}} = P_{\mathrm{HJ}}^{0} + P_{\mathrm{HJ}}^{sc}, \tag{1}$$

where the voltage across the organic is

$$V_O = V_O^0(x) + V_O^{sc}(x). \tag{2}$$

Here, P_{HJ}^0 and V_O^0 are the interface hole density and voltage across the organic at equilibrium [Eq. (9), Paper I], and x is the position within the organic layer relative to the hole injecting contact. The interface hole density and voltage across the organic due to space-charge-limited transport are P_{HJ}^{sc} and $V_O^{sc}(x)$, respectively.

The space-charge model is derived by combining the drift equation, $J = q\mu_O P_O^{sc} F_O$, and Poisson's equation, $\nabla\cdot F_O = qP_O^{sc}/\varepsilon_O$, assuming a low density of intrinsic carriers throughout the organic layer [26]. Here, ε_O is the dielectric permittivity of the organic and q is the electron charge. Further, the organic mobility, μ_O, is assumed to be independent of electric field, F, which has been shown to be accurate at low fields [23]. From these assumptions, we obtain the electric field, the space-charge voltage, and the space-charge carrier density through the organic layer:

$$F_O(x) = \sqrt{\frac{2Jx}{\varepsilon_O\mu_O} + F_c^2}, \tag{3}$$

$$V_O^{sc}(x) = \frac{\varepsilon_O\mu_O}{3J}\left[\left(\frac{2Jx}{\varepsilon_O\mu_O} + F_c^2\right)^{3/2} - F_c^3\right], \tag{4}$$

and

$$P_O^{sc}(x) = \frac{J}{q\mu_O}\frac{1}{\sqrt{\frac{2Jx}{\varepsilon_O\mu_O} + F_c^2}}. \tag{5}$$

Here F_c is the electric field at the injecting contact. Setting $F_c = 0$ reduces Eq. (4) to the Mott-Gurney law [27].

Equation (1) can be used to relate P_{HJ} to the change in quasi-Fermi level across the organic layer $\Delta E_{f,p}$ via

$$P_{\mathrm{HJ}} = P_{\mathrm{HJ}}^0 + P_{\mathrm{HJ}}^{sc} = P_c' \exp\left(\frac{qV_O}{k_BT}\right)\exp\left(-\frac{\Delta E_{f,p}}{k_BT}\right). \tag{6}$$

Here, P_c' is the hole density at the anode when $J \neq 0$, and is related to P_c (the value at $J = 0$) by $P_c' = P_c + J/q\mu_O F_c$. Also, k_B is Boltzmann's constant and T is the temperature. Thus

$$\Delta E_{f,p} = qV_O^0 + qV_O^{sc} - k_BT\ln\left[\frac{P_{HJ}^{sc}}{P_c'} + \frac{P_c}{P_c'}\exp\left(\frac{qV_O}{k_BT}\right)\right]. \tag{7}$$

A. Wide-band gap inorganic semiconductor junctions

To express the dependence of current density on voltage for the wide-band gap diode, we assume an exponential density of trap states in both the organic and inorganic semiconductors [Eq. (11), Paper I], drift-limited transport through the organic at high current, and a small binding energy for the HCTE. Furthermore, by assuming that the current is determined by free carrier recombination with trapped carriers, we can write [cf. Eq. (20), Paper I]

$$J = q\langle a\rangle\left\{k_{\mathrm{rec},n}N_cH_O\exp\left(-\frac{\alpha_O}{k_BT}\right)\left[\exp\left(\frac{qV_a-\Delta E_{f,p}}{n_Ok_BT}\right)-1\right] + k_{\mathrm{rec},p}N_{\mathrm{HOMO}}H_I\exp\left(-\frac{\alpha_I}{k_BT}\right)\left[\exp\left(\frac{qV_a-\Delta E_{f,p}}{n_Ik_BT}\right)-1\right]\right\} - qJ_X + J_I. \tag{8}$$

Here $\langle a\rangle$ is the radius of the HCTE, $k_{\mathrm{rec},n}$ and $k_{\mathrm{rec},p}$ are the free carrier recombination rates, N_{HOMO} and N_c are the densities of states of the highest occupied molecular orbital (HOMO) of the organic and at the conduction band minimum of the inorganic, respectively, H_O and H_I are the organic and inorganic trap densities of states, J_X is the exciton flux from the organic layer to the OI-HJ, and J_I is the photogenerated minority carrier current injected from the inorganic valence band into the organic layer. Given the large band gap energy of TiO_2 (3.3 eV) [2], we can illuminate the TiO_2/DBP diode at energies where only the DBP absorbs (3.3–1.8 eV) [28], thereby generating excitons only in the organic. Under these conditions $J_I = 0$. The ideality factors

(n_O and n_I) and energies (α_O and α_O) are defined in Paper I [Eqs. (14)–(17)]. Along with $\Delta E_{f,p}$, these variables are functions of δ_O and δ_I, the fractions of voltage dropped across the organic and inorganic layers, respectively.

The uniform field approximation is used to determine δ_O and δ_I, which is valid when both the inorganic and the organic regions are fully depleted, consistent with the fact that TiO_2 is undoped and thinner than the depletion width [29]. Under these conditions, the voltage distribution is determined by the ratio of the dielectric constants and layer thicknesses of the organic and inorganic layers.

For simplicity, Eq. (8) is then rewritten:

$$J = J_{s1}\exp\left(-\frac{\alpha_O}{k_BT}\right)\left[\exp\left(\frac{qV_a-\Delta E_{f,p}}{n_Ok_BT}\right)-1\right] + J_{s2}\exp\left(-\frac{\alpha_I}{k_BT}\right)\left[\exp\left(\frac{qV_a-\Delta E_{f,p}}{n_Ik_BT}\right)-1\right] - qJ_X. \tag{9}$$

Here J_{s1} and J_{s2} are functions of k_{rec}, which can be temperature and light intensity dependent.

B. Moderate-band gap inorganic semiconductor junctions

The J-V characteristics for the moderate-band gap inorganic semiconductor diode are obtained by assuming a discrete trap state (at energy E_t from the Fermi energy, $E_{f,n}$) at the inorganic surface. Due to the smaller energy level offsets at the OI-HJ expected in cases where the organic and inorganic energy gaps are comparable, thermionic emission over the interface barrier can also be significant. Assuming that the current is determined by both trapped electron-to-free-hole recombination and thermionic emission over the OI-HJ barrier, then Eqs. (20) and (A1) in Paper I can be combined to obtain

$$\begin{aligned} J = {} & q\langle a\rangle k_{\mathrm{rec}.p}N_{\mathrm{HOMO}}H_I\exp\left(-\frac{E_t}{k_BT}\right)\left[\exp\left(\frac{qV_a-\Delta E_{f,p}}{n_Ik_BT}\right)-1\right] \\ & + \upsilon q a_O P_c\exp\left(-\frac{\Delta E_V}{k_BT}\right)\exp\left(\frac{qV_a}{n_{\mathrm{therm}}k_BT}\right) - qJ_X + J_I. \end{aligned} \tag{10}$$

Here, υ is the attempt frequency to traverse the OI-HJ barrier from the organic to the inorganic, P_c is the hole density at the anode, n_{therm} is the thermionic emission ideality factor that depends on the existence of interface traps, and ΔE_V is the offset between the valence band maximum of the inorganic and the HOMO of the organic. In writing the first exponential of Eq. (10) we have ignored carrier recombination in the bulk of the InP. This is reasonable for photogenerated and injected carriers when thermionic emission is absent since InP has a minority carrier diffusion length (typically $>5\ \mu$m) [18], greater than the thickness used in the device (1 μm). Further we have assumed that when thermionic emission over the barrier is present, the diffusion current dominates over drift at small forward bias.

In the case of interface recombination, $\Delta E_{f,p}$ is again a function of δ_O and δ_I, which are in turn functions of the applied voltage since the InP layer is not fully depleted. At equilibrium, δ_O and δ_I can be determined as followed: First a voltage drop across the inorganic is assumed, and Poisson's equation is used to determine the resulting field at the inorganic side of the OI-HJ. Then the field at the organic side of the OI-HJ is determined using continuity in the electric displacement, and the resulting voltage across the organic is calculated by using the uniform field approximation [see Eqs. (23) and (24), Paper I]. This calculation can be repeated at every voltage to calculate δ_O and δ_I as functions of V_a.

Simplifying Eq. (10), we thus obtain

$$\begin{aligned} J = {} & J_{s1}\exp\left(-\frac{E_t}{k_BT}\right)\left[\exp\left(\frac{qV_a-\Delta E_{f,p}}{n_Ik_BT}\right)-1\right] \\ & + J_{s2}\exp\left(-\frac{\Delta E_V}{k_BT}\right)\exp\left(\frac{qV_a}{n_{\mathrm{therm}}k_BT}\right) - qJ_X + J_I. \end{aligned} \tag{11}$$

III. EXPERIMENT

The thin film TiO_2/DBP devices are grown on a solvent cleaned [30], 150-nm-thick film of indium tin oxide (ITO, Luminescence Technology Corp.) patterned into 1-mm wide stripes on a glass substrate. The device structure is ITO (150 nm)/TiO_2 (60 nm)/DBP (30 nm)/MoO_3 (15 nm)/Al (100 nm) as shown in the inset of Fig. 2. We include a MoO_3 hole transport layer that also protects the DBP from damage during metal deposition. The MoO_3 is capped with an Al cathode to form an Ohmic contact [31,32].

The TiO_2 film is grown by sputtering from a Ti target at 6 SCCM (cubic centimeters per minute at STP) of O_2 flow [33] while maintaining the chamber pressure at 5.5 mTorr. This O_2 flow rate is at the threshold of complete target oxidization determined by the increase in sputtering voltage at a dc power of 300 W [34]. The substrate is heated to 300 °C during deposition at a rate of 0.33 Å/s to promote the formation of a dense and conductive TiO_2 film. The resulting film is determined to be nearly stoichiometric by x-ray photoelectron spectroscopy. Next we sequentially deposit DBP (Luminescence Technology Corp.), MoO_3 (Alfa Aesar), and Al by vacuum thermal evaporation at 1 Å/s in a chamber with a base pressure of 1×10^{-6} Torr. Prior to growth all organics were purified once by vacuum thermal-gradient sublimation. The Al cathode is deposited perpendicular to the ITO stripes through a shadow mask with 1-mm wide openings to define a (1 mm)^2 device area.

Fabrication of the InP/PEN device starts with the growth of a 1000-nm-thick, nominally undoped (1×10^{16} cm^{-3}) InP layer by molecular beam epitaxy on a S-doped (1×10^{18} cm^{-3}) (100) InP wafer (WaferTech LLC). The device structure is InP/PEN (30 nm)/MoO_3 (10 nm)/Au (15 nm) as shown in the inset of Fig. 2. Postgrowth, the wafer is transferred to an e-beam chamber, where an Ohmic contact [Pd

(5 nm)/Ge (50 nm)/Au (65 nm)/Ti (20 nm)/Au (50 nm)] [35] is deposited on the nonepitaxial growth side, followed by annealing in air at 180 °C for 25 min. Prior to organic deposition the wafer is cleaved into $(1.5\ \mathrm{cm})^2$ substrates and the native oxide is removed by brief immersion in buffered HF, rinsing in deionized water, and followed by immediate transfer of the substrate into a glovebox filled with ultrahigh-purity (<1 ppm O_2) N_2. There, the substrate is attached to a Au-coated Si wafer using In to allow access to the cathode. Next, PEN (Sigma Aldrich) and MoO_3 are thermally evaporated in vacuum at 1–2 Å/s. The circular device area of 1 mm radius is defined by a Au cathode deposited through a shadow mask by *e*-beam evaporation. A significant variation in the J-V and EQE characteristics of devices on a single substrate were observed, possibly due to irregular PEN surface morphology resulting from local crystallization commonly observed for this material [36]. For measurements, therefore, we select the devices with the most stable J-V and EQE characteristics vs T.

For temperature-dependent measurements, the devices are loaded into an open-cycle liquid N_2 cryostat. The J-V characteristics are obtained in the dark and under illumination using a semiconductor parameter analyzer. The light intensity is calibrated using a National Renewable Energy Laboratory–traceable Si reference cell. The EQE measurements are obtained with a monochromated (spectral resolution of ∼10 nm) halogen lamp chopped at 200 Hz and a lock-in amplifier. A National Institutes of Standards and Technologies–traceable Si photodetector is used to calibrate the intensity at each wavelength. During measurement, the cryostat is maintained at <1 mTorr to prevent degradation by exposure to oxygen or moisture.

The samples are cooled to 134 K and allowed to equilibrate for 1 h. The measurements are then taken at 20 K steps using a

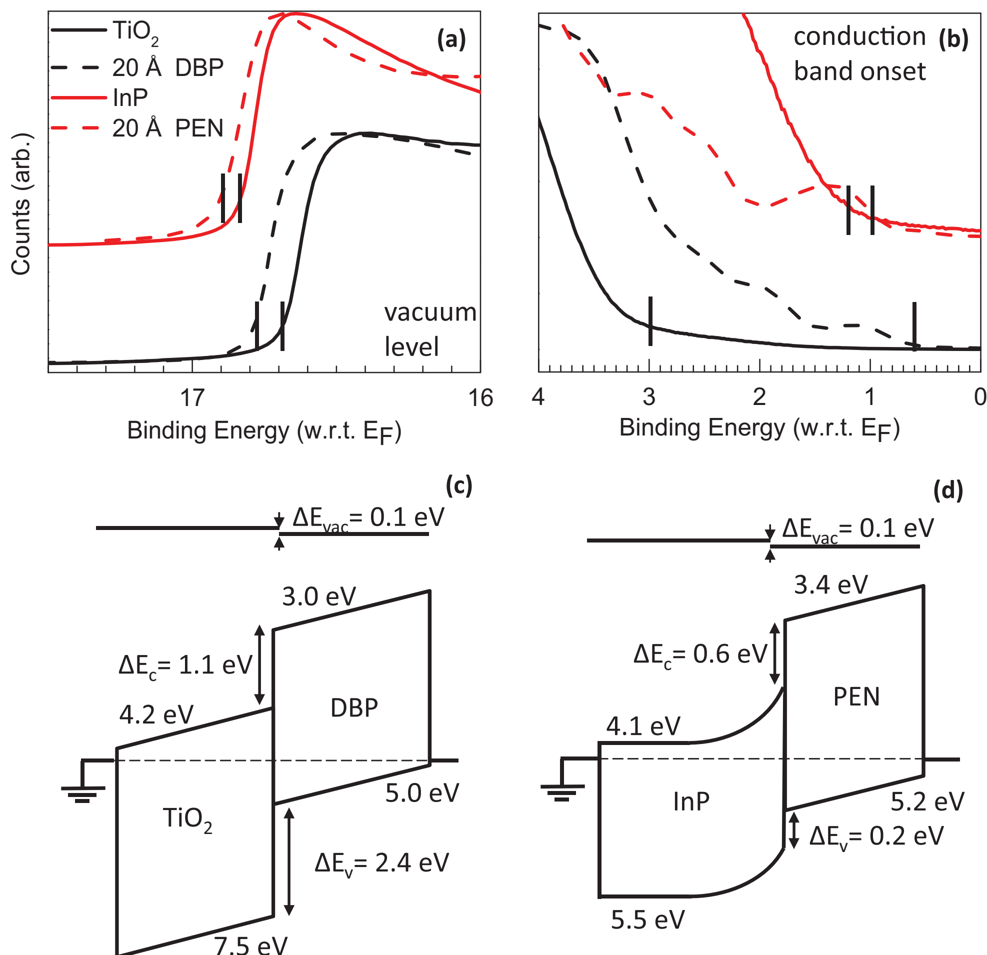

FIG. 3. (Color online) Ultraviolet photoelectron spectra (UPS) of (a) TiO_2 (bottom, solid line), TiO_2 with a 20-Å-thick DBP film (bottom, dashed), InP (top, solid) and InP with a 20-Å-thick PEN film (top, dashed). The short vertical line marks represent the secondary emission cutoff extracted from the spectra (16.7, 16.8, 16.8, and 16.9 ± 0.1 eV, respectively). (b) The low-binding-energy region providing information about the ionization potentials. The short vertical lines indicate the valence band/highest occupied molecular orbital level onset energies (3.0, 0.6, 1.2, and 1.0 ± 0.1 eV, respectively). (c) Equilibrium energy level diagrams of the TiO_2/DBP (d) and InP/PEN OI-HJs inferred from the UPS data. The conduction band and lowest unoccupied molecular orbital levels are estimated from a combination of the UPS data and the optical gaps. Here, ΔE_{vac} is the interface dipole energy in vacuum. Also, ΔE_c and ΔE_V correspond to the energy level offsets at the conduction and valence levels, respectively, and the Fermi level is indicated by the dashed line.

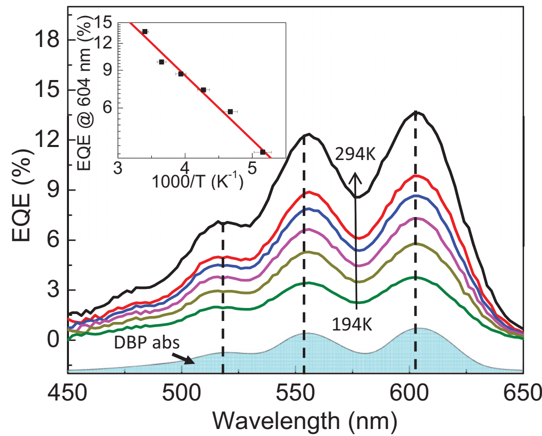

FIG. 4. (Color online) External quantum efficiency (EQE) vs wavelength at several temperatures (T) of a TiO_2/DBP OI-HJ device. The vertical dashed lines indicate the peak positions of the several DBP vibronics. Also shown for reference is the DBP absorption spectrum (shaded region). The data are taken at 20 K intervals. Inset: The EQE at a wavelength of 604 nm is plotted vs $1000/T$. Fit to the data (solid line) yields an activation energy of $\Delta E_{\mathrm{EQE}} = 77 \pm 10$ meV.

thermally controlled stage heater at 20-min intervals to allow for thermal stabilization. To minimize trap-induced hysteresis in the J-V characteristics apparent at low temperatures, the devices are first maintained at 0 V for 5 s before voltage sweeps in both forward and reverse directions. The J-V characteristics under illumination are taken under a power of 100 mW/cm^2 for the TiO_2-based sample, and 25 mW/cm^2 for the InP-based sample. The TiO_2 sample is illuminated at a wavelength of $\lambda = 633$ nm via emission from a He-Ne laser, while the InP sample is illuminated by a AM 1.5G solar simulator. Fits to the data use MATLAB with a nonlinear least-squares, trust-region algorithm.

Photoemission spectroscopy measurements are done in an ultrahigh-vacuum chamber (base pressure $<1 \times 10^{-9}$ Torr) using the 21.22-eV He-I emission from a gas-discharge lamp. The substrates are prepared similarly to those used for device fabrication, and transferred into the system through a N_2-filled glovebox where the organic is deposited in an organic molecular beam deposition system ($\sim 1 \times 10^{-8}$ Torr) interconnected with the measurement chamber [37]. The spectra are collected using a hemispherical electron energy analyzer (Thermo VG) with a pass function full width at half maximum of 0.16 eV.

IV. RESULTS

Figure 2 shows representative room temperature J-V characteristics of both OI-HJ diodes. They exhibit pronounced rectification with an exponential increase in current under forward bias, and stable reverse bias characteristics with breakdown voltage ranging from -15 to -20 V.

Figure 3 shows the ultraviolet photoelectron spectra (UPS) for the two OI-HJs (top) and the equilibrium energy level diagrams inferred from these data (bottom). Figure 3(a) shows the high-binding-energy region of the inorganics, and of the inorganics with a 20-Å organic film deposited on top. From the spectra we determine dipoles of 0.1 ± 0.1 eV at both the TiO_2/DBP and the InP/PEN interfaces. Figure 3(b) shows the low-binding-energy region of the spectra for the two systems, from which we infer the valence band and HOMO energies and their alignments. We estimate the conduction band and lowest unoccupied molecular orbital (LUMO) energies by adding the optical gap to the valence band and HOMO energies [2,28,19,38] to infer 2.4 ± 0.1 eV (1.1 ± 0.1 eV) offset energies between the conduction (valence) band of TiO_2 and the HOMO (LUMO) of DBP. For the InP/PEN OI-HJ, the valence band (conduction band) offset is considerably smaller, at 0.2 ± 0.1 eV (0.6 ± 0.1 eV). Analysis of the UPS data, summarized in the equilibrium energy level diagrams shown in Figs. 3(c) and 3(d), indicates that both systems form type II OI-HJs. In constructing the energy level diagram for TiO_2/DBP, we have assumed a uniform field throughout the structure since both the organic and inorganic are fully depleted. For the InP/PEN, we assume the organic is fully depleted while the field extends only a few microns into the moderately doped InP.

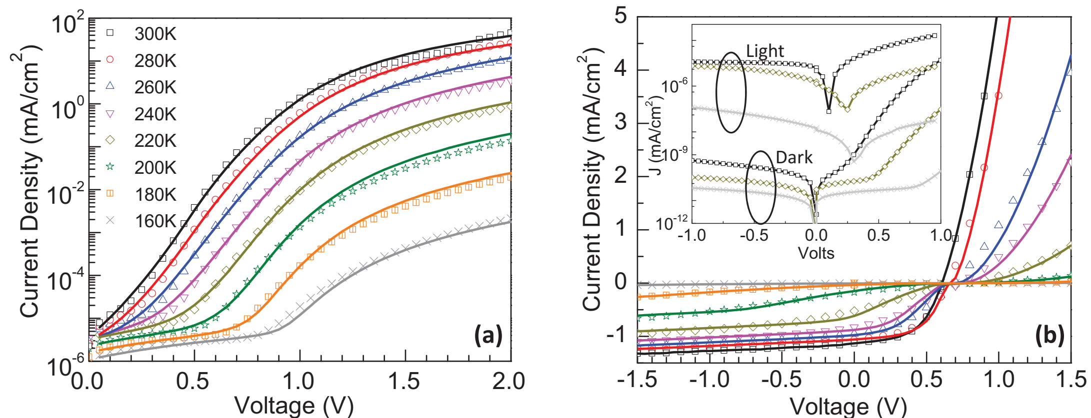

FIG. 5. (Color online) Current density vs voltage (J-V) characteristics at several different temperatures for a TiO_2/DBP OI-HJ device (a) in the dark and (b) under illumination. Data are shown by symbols and fits by lines. Inset: Dark and illuminated J-V characteristics replotted on a log scale at temperatures of 160, 220, and 300 K starting from the bottom.

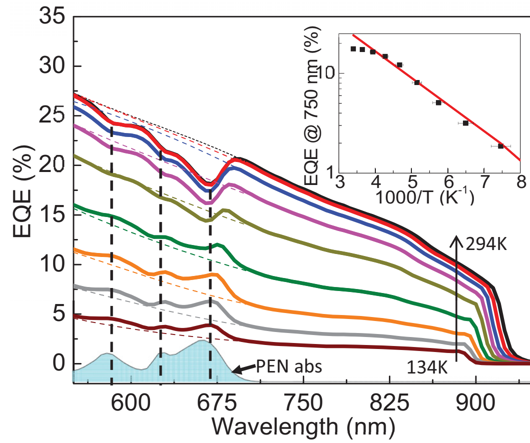

FIG. 6. (Color online) External quantum efficiency (EQE) of a InP/PEN OI-HJ device vs temperature (T) (solid lines) along with the spline fit (dashed lines) used to estimate the InP background. PEN absorption is also shown for reference (shaded region). The vertical dashed lines indicate the peak positions of the several PEN vibronics. Inset: EQE at a wavelength of 750 nm vs $1000/T$ yields an activation energy of $\Delta E_{\mathrm{EQE}} = 55 \pm 10$ meV.

A. Wide-band gap inorganic semiconductor junctions

The EQE of the TiO_2/DBP device as a function of temperature is shown in Fig. 4. The shape of the EQE spectra in the range 450 nm $< \lambda <$ 650 nm matches that of the DBP absorption (also shown), since the wide-band gap TiO_2 is transparent at $\lambda > 375$ nm. At room temperature, the EQE peaks at 13% at $\lambda = 600$ nm and decreases to 4% at $T = 194$ K. The shape of the EQE spectrum does not change with temperature, although its magnitude decreases monotonically. The inset shows an Arrhenius plot of the EQE at $\lambda = 604$ nm, which yields an activation energy of $\Delta E_{\mathrm{EQE}} = 77 \pm 10$ meV.

The J-V characteristics in the dark are shown in Fig. 5(a). They exhibit a pronounced roll-off at $V_a > 1$ V due to space charge, departing from an exponential increase. The onset voltage for roll-off decreases with decreasing T. At low currents there is an exponentially increasing plateau region that resembles a diode with a very high ideality factor. The J-V behavior of the plateau is symmetric about 0 V. The illuminated J-V characteristics are shown in Fig. 5(b). At $V_a > V_{\mathrm{OC}}$ (where V_{OC} is the open circuit voltage), the photocurrent decreases with temperature, similar to the dark current. The photocurrent is symmetric around V_{OC} [inset of Fig. 5(b)]. The fill factor (FF) and power conversion efficiency also decrease with T due to a reduction in photocurrent in the fourth quadrant. The saturated photocurrent at reverse bias, $V_a < -1$ V also decreases with decreasing temperature. A temperature-independent linear slope in photocurrent is observed at high reverse bias, and has been shown previously to be due to photoconductivity of the organic layer [39].

B. Moderate-band gap inorganic semiconductor junctions

The EQE vs T data for the InP/PEN OI-HJ are shown in Fig. 6. The shape of the PEN absorption, consisting of three vibronics within the wavelength interval of $\lambda = 550$ to 700 nm is also shown (shaded region). The EQE at wavelengths outside of the PEN absorption decreases uniformly with temperature, with the long-wavelength cutoff decreasing from $\lambda = 925$ to 900 nm, consistent with the behavior of direct-band gap semiconductors [18]. The inset shows the magnitude of the EQE at $\lambda = 750$ nm vs $1/T$, yielding an activation energy of $\Delta E_{\mathrm{EQE}} = 55 \pm 10$ meV. Within the PEN absorption region, the spectra show three dips at high temperature, and then emerge as peaks as T is reduced.

The forward biased J-V characteristics in the dark are shown in Fig. 7(a), and exhibit an exponential increase of current with applied voltage. Unlike the wide-band gap case, the roll-off follows an Ohmic (i.e., $J \propto V_a$) behavior at high forward bias. The illuminated J-V curves are shown in Fig. 7(b). At $V_a > V_{\mathrm{OC}}$, the forward current behaves similarly to its dark current characteristic, whereas at $V_a < V_{\mathrm{OC}}$ it has an S-kink similar to the illuminated TiO_2/DBP characteristics. The FF and efficiency also decrease with temperature. The saturated photocurrent under reverse bias at each temperature increases linearly with voltage due to the photoconductivity of the PEN layer.

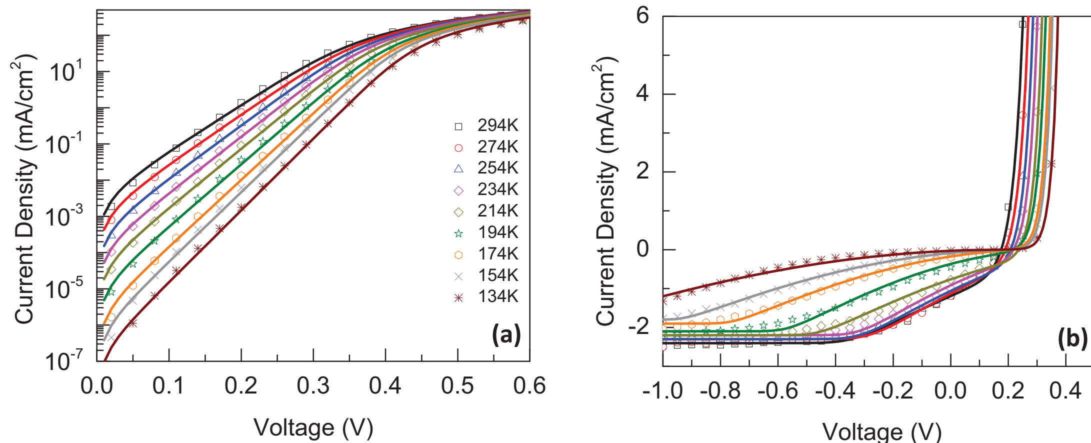

FIG. 7. (Color online) Current density vs voltage characteristics at several different temperatures for an InP/PEN OI-HJ device (a) in the dark and (b) under illumination. Data are shown by symbols and fits by lines.

V. DISCUSSION

The EQE spectra for both the TiO_2/DBP and InP/PEN diodes show evidence of excitons that diffuse to the OI-HJ forming an HCTE and subsequently dissociate to contribute to the photocurrent. However, the behavior of the HCTE with temperature is strikingly different in the two cases.

In the wide-band gap case, the lack of overlap in the absorption spectra of the organic and inorganic unambiguously shows the contribution of DBP excitons to the photocurrent in the EQE spectra of Fig. 4. Since the measured EQE is approximately 100 times higher than a Au (100 nm)/DBP (100 nm)/ITO (72 nm) photoconductor, we conclude that the high EQE of the OI-HJ is due to exciton diffusion to the interface and subsequent dissociation into free charge. The peak magnitude of the EQE decreases with an activation energy of $\Delta E_{\mathrm{EQE}} = 77 \pm 10$ meV (see inset, Fig. 4). The temperature activation of the EQE can result from a decrease in the charge collection efficiency, in the exciton flux to the interface, or in the HCTE dissociation efficiency. Although the HCTE becomes increasingly stable at reduced temperatures, over this temperature range it is not expected to change sufficiently to result in a threefold decrease in EQE. Furthermore, its low binding energy of $\sim$10 meV due to the high dielectric constant of TiO_2 [see Fig. 2(b), Paper I] does *not* correspond to the measured ΔE_{EQE}. Thus, we infer that the observed temperature activation results from a trade-off between the exciton flux to the interface and the charge collection efficiency. Fits to the J-V characteristics of the TiO_2/DBP junction (Sec. V B) yield $\Delta E_{\mathrm{EQE}} = 40 \pm 10$ meV for the exciton flux to the interface. This suggests that at $V_a = 0$ V, the built-in voltage and mobility of the DBP are sufficiently high that the EQE decrease with temperature is due to a reduction in exciton flux to the OI-HJ.

In contrast to the wide-band gap case, the PEN and InP EQE spectra fully overlap, and the excitonic contribution to the EQE is evident only at lower temperature. That is, at high temperature, the EQE in the spectral region of the PEN absorption results in a *net loss*, whereas at low temperature the PEN provides an *increase* to the total photocurrent. To clarify the contributions of PEN, we subtract the InP response between $\lambda = 550$ and 700 nm using a spline fit to the background, as shown by the dashed lines in Fig. 6. The total EQE minus the extrapolated background, further normalized by the charge collection efficiency, are shown in Fig. 8. The collection efficiency is obtained by assuming that it is directly proportional to the EQE in the region where only InP absorbs. It is the same for the organic and inorganic since for both, photogenerated charges are lost through recombination at the OI-HJ. Furthermore, the activation energy of the InP EQE is $\Delta E_{\mathrm{EQE}} = 55 \pm 10$ meV (see inset, Fig. 6), which is similar to the activation energy for the PEN mobility of $E_\mu = 71 \pm 10$ meV, obtained from J-V fits (Sec. V B). This indicates that the change in carrier collection efficiency, resulting from the low hole mobility in PEN, is responsible for the temperature activation of the EQE in the region where only InP absorbs.

It is apparent that at high temperatures, PEN excitons recombine after photogeneration in the bulk of the thin film, or they are quenched at the interface due to trap states at the InP surface. Hence, at the highest temperatures, there is

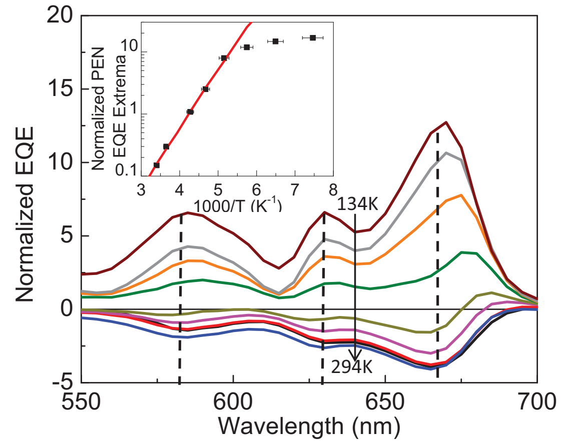

FIG. 8. (Color online) External quantum efficiency (EQE) vs temperature (T) of PEN at 20 K intervals in an InP/PEN OI-HJ. The absolute values of EQE are obtained by subtracting the InP spline fit background in Fig. 6. The EQE contribution from PEN is then referenced to its value at each temperature divided by the background EQE from InP at a wavelength of 750 nm. The vertical dashed lines indicate the peak positions of the several PEN vibronics. Inset: Peak EQE for the 0-0 (lowest energy) vibronic vs $1000/T$, giving an activation energy of $\Delta E_{\mathrm{EQE}} = 0.21 \pm 0.04$ eV.

no change in the absorption signal since nearly all excitons recombine prior to dissociation. However, as temperature is decreased, the loss decreases, eventually resulting in a positive contribution to the photocurrent at $T \leq 214$ K, with the largest increase occurring immediately at the long-wavelength PEN absorption edge. The increase in EQE contributed by PEN is approximately 18% from the highest to lowest temperature. The magnitude of that contribution is nearly as high as that of InP at $T = 134$ K, and in all cases is 20 times higher than the photoconductivity obtained for an Al (15 nm)/PEN (30 nm)/ITO (150 nm) sample. Note too, that the peaks in EQE align with those of the absorption spectra, except near the transition from loss to gain at $T = 214$ K, where there is a small bathochromic shift of the long-wavelength tail of the 0-0 vibronic. This peak progressively shifts back towards the 0-0 vibronic maximum with decreasing temperature as gain dominates over loss. The enhanced contribution near the excitonic absorption edge results since the material at the long-wavelength absorption cutoff is nearly transparent, resulting in uniform illumination and hence exciton generation nearer to the OI-HJ where dissociation becomes dominant over interface recombination. A similar shift is commonly observed in the photoluminescence maxima of semiconductors where the convolution of the emission and absorption spectra result in a maximum at the transparency edge of the medium.

Interestingly, the activation energy of the difference spectra is $\Delta E_{\mathrm{EQE}} = 0.21 \pm 0.04$ eV, and has the *opposite* dependence with temperature compared to the wide-band gap case. This is indicative of the different role that surface states play in the two devices. For TiO_2/DBP, the surface states are not active under the conditions tested, yet for InP/PEN, surface trap occupancy is found to change, reducing the rate of HCTE and/or exciton quenching as the temperature is reduced. Indeed, the activation energy measured is consistent with the position of InP surface

states relative to the Fermi energy, as inferred from Li *et al.* [9]. With the deposition of PTCDA on top of p-InP, they find that the barrier height changes by 9 meV. Adding this to the barrier height obtained from UPS (1.1 ± 0.1 eV) and the InP band gap (1.35 eV), we find that the surface states should be located at 0.26 ± 0.1 eV above the valence band maximum, consistent with our measurement of ΔE_{EQE}.

There is a possibility that Förster transfer from the organic to inorganic semiconductor can bypass the formation of the HCTE in the charge photogeneration process [11]. The FRET probability is proportional to the overlap between the absorption spectrum of InP and photoluminescence (PL) spectrum of PEN [40]. To estimate the probability of Förster transfer from PEN to InP, we measured the PL of a 100-nm-thick PEN film on an oxidized Si substrate vs T. The film was pumped with $\lambda = 337$ nm emission from a N_2 laser at $1.5 \times 10^4\ \mu\mathrm{J/cm^2}$. Similar to Park *et al.* [41] we find the PL exhibits broad features at high energy ($\lambda = 500$ to 750 nm) that do not change significantly with temperature, and two peaks at longer wavelength ($\lambda = 775$ to 925 nm) that increase with decreasing temperature: between 294 and 134 K, the PL in the long-wavelength region increases fivefold. However, at all temperatures, the PL efficiency (η_{PL}) is low, with a maximum of $\eta_{\mathrm{PL}} = 0.013\%$ at 134 K. To quantify the effects of FRET, we calculate the Förster radius using [40,42]

$$R_o^6 = \frac{9\eta_{\mathrm{PL}}\kappa^2}{128\pi^5 n^4}\int \lambda^4 F_D(\lambda)\sigma_A(\lambda)d\lambda, \qquad (12)$$

where κ is the dipole orientation factor, n is the index of refraction of InP, F_D is the normalized fluorescence spectrum of PEN, and σ_A is the absorption cross section of InP. We note that Eq. (12) is valid only for point-dipole to point-dipole coupling. Other approximate solutions exist for point-dipole to near-band-edge transitions in a semiconductor [43]. Using $\kappa = 0.845\sqrt{2/3}$ appropriate for an amorphous film with randomly oriented rigid dipoles [42], we calculate a Förster radius of 4 Å. Hence, the contribution to the EQE at $\lambda = 663$ due to FRET can arise only from excitons located within R_o of the interface. For $L_D \sim 10$ nm and an absorption coefficient of $10^5\ \mathrm{cm^{-1}}$, we obtain the contribution from FRET of <0.01%. We note that this is an *upper limit*, since the first few monolayers of PEN stand normal relative to the substrate plane [44,45]. Thus, their emission dipole moments are oriented such that $\kappa \to 0$ implying that transfer is preferentially in plane, and cannot couple efficiently to the InP substrate as inferred from Eq. (12).

A. *J-V* characteristics: Wide-band gap semiconductor junctions

In this section and in Sec. V B, we apply the theory in Paper I to modeling the J-V characteristics of our two archetype OI-HJ systems. As in all fits to J-V data, several parameters emerge whose values provide insight into the detailed dynamics of the devices studied. We find excellent fits to the data for both systems under reverse and forward bias, as well as illumination conditions and temperature. While the fits provide strong support for our analysis, here the characteristics are primarily used to complete the picture of the formation of an HCTE in both junctions.

TABLE I. Fitting parameters for TiO_2/DBP current-voltage characteristics.

Parameter	Value
$T_{t,O}$	710 ± 80 K
μ_∞	$6 \pm 4\ \mathrm{cm^2/Vs}$
ΔE_μ	0.33 ± 0.06 eV
$J_{s1,\infty}$ (dark)	$8 \pm 4\ \mathrm{A/cm^2}$
E_a (dark)	0.19 ± 0.01 eV
J_{s1} (light)	$80 \pm 24\ \mathrm{mA/cm^2}$

Equation (9) is used to fit the J-V characteristics of the TiO_2/DBP junction in the dark and under illumination in Figs. 5(a) and 5(b), respectively. For fits to the dark J-V characteristics we use J_{s1},μ and $T_{t,O}$ as parameters. Furthermore, we vary J_{s1} and μ with temperature, since $J_{s1}(T)$ is a function of $k_{\mathrm{rec}}(T)$, which in turn is proportional to $\mu(T)$. For the J-V fits under illumination, we also use the parameters from the fit in Fig. 5(a), but recognize that the k_{rec} can also depend on light intensity, and that J_X is a function of the temperature-dependent exciton diffusion in disordered organic thin films. For the fits, we take the approximate experimental values of $\varepsilon_O = 4\varepsilon_o$, $V_{bi} = 0.5$ V, and an injection barrier at the cathode and anode of $\phi_{c,a} = 0.2$ eV. Here, ε_0 is the permittivity of free space. Finally, we note that since the currents in the low forward current plateau region in Fig. 5(a) are small (<100 pA), they can be influenced by artifacts such as the long time constants of trapped carriers or dielectric leakage in the probes contacting the device. Therefore, the reliability of the fits corresponding to the second term of Eq. (10) is reduced by these measurement inaccuracies. The fit results are shown by lines in Fig. 5, with the parameters used provided in Table I.

From these fits, we find that the hole mobility, $\mu(T) = \mu_\infty \exp(-\frac{\Delta E_\mu}{kT})$, where μ_∞ is the mobility at high temperature, and the thermal activation energy is $E_\mu = 0.33 \pm 0.04$ eV [see Fig. 9(a)] as inferred from the space-charge roll-off region of the forward characteristics in Fig. 5. This magnitude of activation energy is consistent with previous measurements of organic films whose charge transport is dominated by polaron hopping between discrete sites with energetic disorder [46,47].

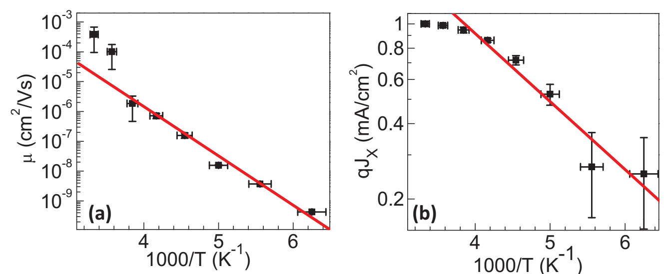

FIG. 9. (Color online) (a) Mobility vs temperature ($1000/T$) obtained from J-V characteristics of the TiO_2/DBP OI-HJ shown in Fig. 5. An activation energy of $E_\mu = 0.33 \pm 0.06$ eV is obtained from the fit (solid line). (b) Exciton flux to the interface (qJ_X) vs $1000/T$ obtained from the J-V fits under illumination, yielding an activation energy of $\Delta E_{\mathrm{EQE}} = 40 \pm 10$ meV.

To confirm that the space-charge roll-off is due to the properties of DBP, we fabricated a device that replaced TiO_2 with a thin C_{60} layer, with the structure ITO (150 nm)/C_{60} (10 nm)/DBP (30 nm)/MoO_3 (15 nm)/Al (100 nm). Here the C_{60} film has a considerably higher mobility (5.1×10^{-2} $cm^2/V\,s$) [48] than DBP and hence is not current limiting in the test structure. This organic device exhibits a similar thermal activation for the space-charge roll-off as the TiO_2/DBP device, indicating that the observed effects are indeed due to DBP. The thermally activated mobility fully accounts for the decrease in FF vs temperature in the J-V characteristics under illumination in Fig. 5(b). This is apparent in the inset of Fig. 5(b), which provides the data and fit on a semilog scale for selected temperatures. Under illumination, there is surprising symmetry in the current centered about the open-circuit voltage (V_{OC}) (identified by the dip in current where it switches from positive to negative). This symmetry is a result of space-charge effects dominating current transport in both the forward and reverse directions. Thus, at $V > V_{OC}$, holes are injected from the contact and transported to the OI-HJ by drift. At $V < V_{OC}$, the direction of the current is reversed as the photogenerated holes are transported by drift away from the OI-HJ to the anode. In this case, the sign of Eq. (7) is reversed and the field at the contact, F_c, is replaced by the field at the interface, F_{HJ}.

In Paper I, we showed that a reduction in FF can result from field-dependent dissociation of the HCTE state. Accurate fits to FF using Eq. (8), where the binding energy of the HCTE is assumed to be small, suggest that field-dependent dissociation is not dominant. The low HCTE binding energy is further supported by the small value of $\delta_I = 0.22 \pm 0.04$ obtained from the fit. Using the uniform field approximation $\delta_I = \varepsilon_O W_I / \varepsilon_I W_O$. For $\varepsilon_O = 4\varepsilon_o$, we infer that $\varepsilon_I \approx 35\varepsilon_o$. This falls within the range of dielectric constants reported for TiO_2 of from 15 to 250, depending on deposition condition [19–21]. In our case, we measured ε_I via the capacitance of a $(1\ mm)^2$ ITO (150 nm)/TiO_2 (60 nm)/Au (100 nm) sample. The capacitance ranges from 3 to 12 nF, corresponding to $\varepsilon_I/\varepsilon_o \approx 25-100$.

A dependence of J_{s1} on illumination intensity is evident from the inset of Fig. 5(b). From the J-V fit we find that J_{s1} has an activation energy of $E_a = 0.19 \pm 0.01$ eV in the dark, but lacks a pronounced temperature dependence under illumination. From this we infer that k_{rec} is diffusion limited in the dark when carrier density at the interface is low, and therefore both J_{s1} and μ have a similar activation energy. However, when illuminated, the carrier density at the interface is large, such that k_{rec} is limited by the resulting short charge recombination lifetime at the interface, which is expected to be only weakly temperature dependent.

Finally, J_X has an activation energy of $\Delta E_{EQE} = 40 \pm 10$ meV from Fig. 9(b). This results from a reduction in the exciton diffusion length in DBP with temperature, consistent with previous reports for organic materials [49,50].

B. J-V characteristics: Moderate-band gap semiconductor junctions

Equation (11) is used to fit the measured InP/PEN J-V characteristics (data points) in the dark and under illumination, with results (lines) in Figs. 7(a) and 7(b), respectively. In the dark, thermionic emission [second term on the right-hand side of Eq. (11)] dominates. For the illuminated J-V characteristics, the first term on the left-hand side of Eq. (11) dominates when fitting the inflection below $V < V_{OC}$. The fit parameters are summarized in Table II.

TABLE II. Fitting parameters for InP/PEN current-voltage characteristics.

Parameter	Value
μ_∞	3×10^{-5}–2×10^{-6} $cm^2/V\,s$
E_μ	71 ± 10 meV
J_{s2} (dark)	5 ± 4 mA/cm^2
J_s (light)	10^{-10}–10^{-12} mA/cm^2
R_s	0.44 ± 0.02 $\Omega\,cm^2$

The values of saturation current prefactor, J_{therm} [$J_{s2}\exp(-\frac{\Delta E_V}{k_B T})$], obtained from fits to the dark data are shown in Fig. 10(a), with an activation energy of $\Delta E_V = 0.24 \pm 0.04$ eV, which corresponds to the valence energy offset at the OI-HJ. This also agrees with $\Delta E_V = 0.2 \pm 0.1$ eV directly measured by UPS. The fits yield an ideality factor that increases from $n_{therm} = 1.25 \pm 0.01$ at $T = 294$ K to $n_{therm} = 1.96 \pm 0.01$ at $T = 134$ K [see inset, Fig. 10(a)]. This increase with decreasing temperature is due to the increasing importance of recombination at the HJ resulting from a decrease in the probability for injected carriers to surmount the interface barrier. This is also consistent with the behavior of conventional Schottky barrier diodes with temperature [51,52].

The PEN hole mobilities vs T obtained from fits to the illuminated J-V characteristics are plotted in Fig. 10(b), showing $\Delta E_\mu = 71 \pm 10$ meV. To independently determine μ, we measured the dark J-V characteristics of an Au/MoO_3 (10 nm)/PEN (200 nm)/MoO_3 (10 nm)/Au. From this, we estimate an upper limit of $\mu \sim 10^{-6}$ $cm^2/V\,s$, in agreement with the values in Fig. 10(b). The low mobility normal to the substrate arises since the PEN molecular plane typically lies perpendicular to the substrate. This leads to a large anisotropy with the lowest mobility normal to the plane, consistent with measurements [53]. Also, 40-nm-thick PEN film on InP has a root mean square roughness of 10 nm as determined by

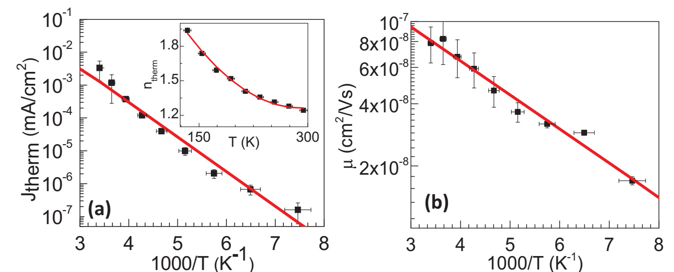

FIG. 10. (Color online) (a) Saturation current vs temperature ($1000/T$) obtained from J-V fits in the dark for an InP/PEN OI-HJ [Fig. 7(a)], yielding an activation energy of $\Delta E_V = 0.24 \pm 0.04$ eV. This corresponds to the valence energy offset at the organic/inorganic heterojunction. Inset: Ideality factor, n_{therm} vs T. (b) Mobility vs $1000/T$ obtained from illuminated current density vs voltage fits. An activation energy of $E_\mu = 71 \pm 10$ meV is obtained from the fit (solid line).

atomic force microscopy. The small E_μ suggests, therefore, that transport is limited by hopping at grain boundaries [24,54] in contrast to the polaron trap-and-release model used to describe the larger E_μ of DBP.

Finally, the illuminated J-V data give a temperature-independent saturation current prefactor, $[J_{s1}\exp(-\frac{E_t}{n_I k_B T})]$, in Eq. (11). From this, we infer that the inflection in the illuminated J-V is due to recombination of electrons trapped in discrete trap states at the inorganic surface with free holes in the organic. For an electron quasi-Fermi level pinned at the OI-HJ by a high density of interface traps [55], the saturation current is expected to be temperature independent, as observed.

VI. CONCLUSIONS

The theory of charge and exciton dynamics at an OI-HJ presented in Paper I is used to describe both the EQE and J-V characteristics of a wide-band gap TiO_2/DBP and a moderate-band gap InP/PEN OI-HJ device. In both cases we find evidence that excitons generated in the organic thin films contribute to the photocurrent through generation of an intermediate hybrid charge transfer exciton state that spans the OI interface. We find that the effects of interface traps are markedly different in these two systems. There is little evidence that traps impact the formation or recombination of HCTEs for the wide-band gap case, whereas in the moderate-band gap case, they dominate HCTE dynamics over a wide range of temperatures. Fits to the J-V characteristics in the dark and under illumination over a wide temperature range provide further validation of the model in Paper I. Both systems form type-II OI-HJs, although with considerably different energy level offsets at the interfaces. From the fits, we find that the magnitude of the OI-HJ energy offsets and the influence of traps at the HJ determine the recombination kinetics of injected and photogenerated carriers. Specifically, in the wide-band gap case, we find that the J-V characteristics both in the dark and under illumination are determined by interface recombination. In the moderate-band gap case, the dark J-V characteristics are determined by thermionic emission into the InP bulk, while under illumination interface recombination dominates. Furthermore, we find that space-charge effects arising from the low mobility of the organic thin film results in a reduction in fill factor as the temperature is reduced.

The framework for understanding the charge generation and recombination dynamics in OI-HJ devices presented here can be extended to include additional processes in nonideal junctions, such as the field dependence of mobility of the organic semiconductor, and Shockley-Reed-Hall generation and recombination statistics in the depletion region of the inorganic semiconductor. Ultimately, the impact of materials and processing parameters on the formation and dissociation of HCTEs remains an important area of investigation to the functioning of numerous modern organic semiconductor-based devices, including colloidal quantum dot and dye sensitized solar cells, organic light emitting diodes, and lasers. The theory and experiments described in Papers I and II provide a starting point from which to understand many aspects of photogeneration and charge transport dynamics in these important applications.

ACKNOWLEDGMENTS

This work was supported in part by Department of Energy, Office of Basic Energy Sciences, as part of Energy Frontier Research Centers: The Center for Solar and Thermal Energy Conversion at the University of Michigan (Award No. DE-SC000957). We acknowledge the University of Michigan's Lurie Nanofabrication Facility for assistance and infrastructure used in device fabrication. A.P. thanks Xiao Liu and Michael Slootsky for help with instrumentation. S.R.F. thanks The Technion, Israel Institute of Technology, for providing support via a Lady Davis Visiting Professorship.

[1] C. K. Renshaw and S. R. Forrest, Phys. Rev. B **90**, 045302 (2014).
[2] B. Oregan and M. Gratzel, Nature **353**, 737 (1991).
[3] A. Hagfeldt, G. Boschloo, L. C. Sun, L. Kloo, and H. Pettersson, Chem. Rev. (Washington, DC, U. S.) **110**, 6595 (2010).
[4] J. Boucle, P. Ravirajan, and J. Nelson, J. Mater. Chem. **17**, 3141 (2007).
[5] S. S. Li and C. W. Chen, J. Mater. Chem. A **1**, 10574 (2013).
[6] M. Slootsky, X. Z. Liu, V. M. Menon, and S. R. Forrest, Phys. Rev. Lett. **112**, 076401 (2014).
[7] S. R. Forrest, M. L. Kaplan, P. H. Schmidt, and J. V. Gates, J. Appl. Phys. **57**, 2892 (1985).
[8] S. R. Forrest, M. L. Kaplan, and P. H. Schmidt, J. Appl. Phys. **60**, 2406 (1986).
[9] N. Li, K. Lee, C. K. Renshaw, X. Xiao, and S. R. Forrest, Appl. Phys. Lett. **98**, 053504 (2011).
[10] V. M. Agranovich, D. M. Basko, G. C. La Rocca, and F. Bassani, J. Phys.: Condens. Matter **10**, 9369 (1998).
[11] G. Heliotis, G. Itskos, R. Murray, M. D. Dawson, I. M. Watson, and D. D. C. Bradley, Adv. Mater. (Weinheim, Ger.) **18**, 334 (2006).
[12] S. Blumstengel, S. Sadofev, and F. Henneberger, New J. Phys. **10**, 065010 (2008).
[13] G. Hughes, J. Roche, D. Carty, T. Cafolla, and K. E. Smith, J. Vac. Sci. Technol. B **20**, 1620 (2002).
[14] G. Salvan and D. R. T. Zahn, Europhys. Lett. **67**, 827 (2004).
[15] A. E. Colbert, E. M. Janke, S. T. Hsieh, S. Subramaniyan, C. W. Schlenker, S. A. Jenekhe, and D. S. Ginger, J. Phys. Chem. Lett. **4**, 280 (2013).
[16] N. Bansal, L X. Reynolds, A. Maclachlan, T. Lutz, R. S. Ashraf, W. Zhang, C. B. Nielsen, I. McCulloch, D. G. Rebois, T. Kirchartz, M. S. Hill, K. C. Molloy, J. Nelson, and S. A. Haque, Sci. Rep. **3**, 1531 (2013).
[17] Y. Vaynzof, A. A. Bakulin, S. Gelinas, and R. H. Friend, Phys. Rev. Lett. **108**, 246605 (2012).
[18] S. M. Sze and K. K. Ng, *Physics of Semiconductor Devices* (Wiley, New York, 2007).
[19] W. Haynes, *CRC Handbook of Chemistry and Physics*, 94th ed. (CRC Press, Boca Raton, FL, 2013).
[20] E. Hendry, F. Wang, J. Shan, T. F. Heinz, and M. Bonn, Phys. Rev. B **69**, 081101 (2004).

[21] E. Yagi, R. R. Hasiguti, and M. Aono, Phys. Rev. B **54**, 7945 (1996).
[22] P.-T. Hsiao, Y.-L. Tung, and H. Teng, J. Phys. Chem. C **114**, 6762 (2010).
[23] M. Pope and C. E. Swenberg, *Electronic Processes in Organic Crystals and Polymers* (Oxford University Press, New York, 1999).
[24] V. Coropceanu, J. Cornil, D. A. da Silva, Y. Olivier, R. Silbey, and J. L. Bredas, Chem. Rev. (Washington, DC, U. S.) **107**, 926 (2007).
[25] S. R. Forrest and F. F. So, J. Appl. Phys. **64**, 399 (1988).
[26] P. Mark and A. M. Lampert, *Current Injection in Solids* (Academic Press, New York, 1970).
[27] M. Nevill and G. Ronald, *Electronic Processes in Ionic Crystals*, 2nd ed. (Dover Publications Inc., New York, 1964).
[28] X. Xiao, J. D. Zimmerman, B. E. Lassiter, K. J. Bergemann, and S. R. Forrest, Appl. Phys. Lett. **102**, 073302 (2013).
[29] U. Diebold, Surf. Sci. Rep. **48**, 53 (2003).
[30] N. N. Wang, J. D. Zimmerman, X. R. Tong, X. Xiao, J. S. Yu, and S. R. Forrest, Appl. Phys. Lett. **101**, 133901 (2012).
[31] M. T. Greiner, M. G. Helander, W.-M. Tang, Z.-B. Wang, J. Qiu, and Z.-H. Lu, Nat. Mater. **11**, 76 (2012).
[32] X. Tong, R. F. Bailey-Salzman, G. Wei, and S. R. Forrest, Appl. Phys. Lett. **93**, 173304 (2008).
[33] B. X. Zhao, J. C. Zhou, and L. Y. Rong, Trans. Nonferrous Met. Soc. China **20**, 1429 (2010).
[34] C. J. Tavares, J. Vieira, L. Rebouta, G. Hungerford, P. Coutinho, V. Teixeira, J. O. Carneiro, and A. J. Fernandes, Mater. Sci. Eng. B **138**, 139 (2007).
[35] G. J. Bauhuis, P. Mulder, E. J. Haverkamp, J. Huijben, and J. J. Schermer, Sol. Energy Mater. Sol. Cells **93**, 1488 (2009).
[36] D. Knipp, R. A. Street, A. Volkel, and J. Ho, J. Appl. Phys. **93**, 347 (2003).
[37] S. R. Forrest, Chem. Rev. (Washington, DC, U. S.) **97**, 1793 (1997).
[38] D. J. Yun, J. Chung, C. Jung, H. S. Han, J. Lee, B. Anass, S. Lee, Y. Kyung, and S. H. Park, J. Electrochem. Soc. **160**, H436 (2013).
[39] C. K. Renshaw, J. D. Zimmerman, B. E. Lassiter, and S. R. Forrest, Phys. Rev. B **86**, 085324 (2012).
[40] T. Forster, Discuss. Faraday Soc. **27**, 7 (1959).
[41] S. P. Park, S. S. Kim, J. H. Kim, C. N. Whang, and S. Im, Appl. Phys. Lett. **80**, 2872 (2002).
[42] S. M. Menke and R. J. Holmes, Energy Environ. Sci. **7**, 499 (2014).
[43] M. Stavola, D. L. Dexter, and R. S. Knox, Phys. Rev. B **31**, 2277 (1985).
[44] H. C. Yang, T. J. Shin, M. M. Ling, K. Cho, C. Y. Ryu, and Z. N. Bao, J. Am. Chem. Soc. **127**, 11542 (2005).
[45] N. Koch, I. Salzmann, R. L. Johnson, J. Pflaum, R. Friedlein, and J. P. Rabe, Org. Electron. **7**, 537 (2006).
[46] D. Hertel and H. Bassler, ChemPhysChem **9**, 666 (2008).
[47] H. Bassler, Phys. Status Solidi B **175**, 15 (1993).
[48] B. P. Rand, J. G. Xue, S. Uchida, and S. R. Forrest, J. Appl. Phys. **98**, 124902 (2005).
[49] O. V. Mikhnenko, F. Cordella, A. B. Sieval, J. C. Hummelen, P. W. M. Blom, and M. A. Loi, J. Phys. Chem. B **112**, 11601 (2008).
[50] F. B. Dias, K. T. Kamtekar, T. Cazati, G. Williams, M. R. Bryce, and A. P. Monkman, ChemPhysChem **10**, 2096 (2009).
[51] H. Cetin and E. Ayyildiz, Semicond. Sci. Technol. **20**, 625 (2005).
[52] M. K. Hudait and S. B. Krupanidhi, Phys. B: Condens. Matter **307**, 125 (2001).
[53] J. Cornil, J. P. Calbert, and J. L. Bredas, J. Am. Chem. Soc. **123**, 1250 (2001).
[54] A. Di Carlo, F. Piacenza, A. Bolognesi, B. Stadlober, and H. Maresch, Appl. Phys. Lett. **86**, 263501 (2005).
[55] E. Hokelek and G. Y. Robinson, J. Appl. Phys. **54**, 5199 (1983).